PAPER

Check for updates

X-ray irradiation effects on Egyptian blue and green pigments†

Marie Godet, ‡*[a] Laurent Binet,[b] Sebastian Schöder,[c] Lucile Brunel-Duverger,[d] Mathieu Thoury[a] and Loïc Bertrand *[ae]

Egyptian blue and green are among the oldest synthetic pigments produced by humanity. The two pigments are complex multi-phase copper-based systems synthesised with different protocols from the same raw materials. Since the 2000s, synchrotron X-ray techniques have provided significant new insights on their chemistry and microstructure. However, the potential impact of high flux irradiation of these pigments has not yet been studied despite the fact that it can lead to visual discoloration and less readily observable alterations such as defects formation or redox changes. In this work, we investigate the effects of synchrotron X-ray irradiation on Egyptian blue and green samples. Radiation-induced effects are monitored after irradiation at increasing doses using electron paramagnetic resonance (EPR) spectroscopy at temperatures of 290 K and 30 K. The cupric ion (Cu^{2+}) is in D_{4h} axial geometry in Egyptian blue and in disordered geometry in Egyptian green, which makes the two pigments very easily identifiable by EPR. Egyptian green samples are found to be much more sensitive to X-rays than Egyptian blue. In particular, a browning of the green samples is observed from the lowest doses tested while no color change is detected for the blue ones. Three types of radiation-induced defects are detected after irradiation: E', non-bonding oxygen hole and aluminum hole centers. Correlations between defect intensity and dose are calculated. Archaeological and modern pigments (whether blue or green) do not show the same reactivity to X-rays, which opens the prospect of using radiation-induced defects as a marker of their history.

1 Introduction

Blue and green colors are very present in the Nilotic landscape, which gives them an important place in the productions of ancient Egypt.[1] At least as early as in the 4th Dynasty (2613–2494 BC),[2] Egyptian craftsmen looked for substitutes to blue and green natural pigments and invented Egyptian blue, the first known synthetic pigment produced by humanity,[3] followed by Egyptian green several centuries later in the 11th Dynasty (2130–1991 BC).[4] Egyptian blue was the most extensively used

blue pigment in Antiquity.[5] During the Middle Ages, it was gradually replaced by other blue pigments such as lapis-lazuli in Europe,[6] although it was still occasionally found on works of art until the 16th century.[7,8] Egyptian green seems to have been of use only in Egypt and until the 21st Dynasty (1069–945 BC).[4] Both pigments were found to decorate many art objects such as coffins, pottery, mural paintings, *etc.*[9–11] In the 18th and 19th centuries, the excavations in Pompeii as well as the French Campaign in Egypt led to a renewed interest in Egyptian blue. Several European chemists took up the challenge of analyzing the pigment and reproducing the ancient manufacturing process.[12,13] Thereafter, Egyptian blue has never ceased to be studied following the development of inorganic analytical chemistry. Detailed reviews of the pigment history up to the 2000s can be found in Riederer[5] (1997) or Baraldi *et al.*[14] (2001).

Previous studies determined that Egyptian blue and green are multi-component systems synthesized from the same raw materials but obtained with different protocols. The raw materials include a copper-based ingredient (malachite, cuprite, metallic copper, bronze waste), silica (quartz sand, crushed quartz pebbles), a calcium-based compound (limestone, shell, calcareous sand) and an alkaline flux (natron, evaporated river water residues, vegetable ashes). The ingredients are mixed in variable proportions (with a higher amount of flux for the green which will

[a]*Université Paris-Saclay, CNRS, ministère de la Culture, UVSQ, MNHN, IPANEMA, F-91192 Saint-Aubin, France. E-mail: msgodet@gmail.com*

[b]*Chimie ParisTech, PSL Research University, CNRS, Institut de Recherche de Chimie Paris (IRCP), F-75005 Paris, France*

[c]*SOLEIL synchrotron, F-91192 Saint-Aubin, France*

[d]*Centre de Recherche et de Restauration des Musées de France (C2RMF), F-75001 Paris, France*

[e]*Université Paris-Saclay, ENS Paris-Saclay, CNRS, Photophysique et Photochimie Supramoléculaires et Macromoléculaires, F-91190 Gif-sur-Yvette, France. E-mail: loic.bertrand@ens-paris-saclay.fr*

† Electronic supplementary information (ESI) available: Characterization of Egyptian blue and green samples using SEM-EDX, XRD, synchrotron XRF and EPR (PDF). See https://doi.org/10.1039/d2ja00020b

‡ Present address: Laboratoire de recherche des monuments historiques (LRMH), 29 rue de Paris, 77420 Champs-sur-Marne, France.

favor the formation of an amorphous phase) and fired at 850–1080 °C for the Egyptian blue and 950–1150 °C for the Egyptian green.[15,16] Egyptian blue contains mostly calcium-copper tetrasilicate $CaCuSi_4O_{10}$ (cuprorivaite) crystals, partially reacted silica phases (quartz, trydimite) and a copper-bearing glassy phase. Wollastonite $CaSiO_3$ and other siliceous phases are detected as impurities.[17–20] Egyptian green was (and is still) far less known and less studied than its blue counterpart, probably because its use was limited to Egypt and because most of the studies published about it were in German.[21] Egyptian green is mainly constituted of a copper-rich amorphous silicate phase entrapping copper-bearing wollastonite $(Ca_xCu_{1-x})SiO_3$ crystals and silica compounds (quartz, trydimite, cristobalite).[15,22–24]

Since the 2000s and the development of synchrotron techniques in heritage sciences, new insights have been obtained on the Egyptian palette, especially on Egyptian blue and green. Synchrotron sources produce high-energy X-ray beams whose properties make it a useful probe for analyzing heterogeneous materials on several scales and for providing information on their chemistry, origin, elaboration or alteration processes.[25] In particular, Pagès-Camagna *et al.*[26] have used extended X-ray absorption fine structure (EXAFS) spectroscopy to determine the Cu^{2+} chromophore local geometry in Egyptian blue and green. Provenance studies were conducted through synchrotron-based X-ray fluorescence (XRF)[27] or X-ray absorption near edge structure (XANES) spectroscopy.[28,29] High temperature X-ray diffraction (XRD) measurement demonstrated that cuprorivaite crystals nucleate and grow within a liquid or glassy phase.[30]

High doses deposited by synchrotron X-ray irradiation can lead to the creation of defects and radicals, loss of crystallinity and redox modifications that change the atomic structure and thus the material properties. The issue of such radiation damage has only been recently addressed in the field of ancient materials (see Bertrand *et al.*[31] and references therein). Changes at the atomic scale often lead to undesirable visual discoloration, as for pigments,[32,33] paper,[34] textiles[35] or fossils.[36] In many cases, radiation damage is not detectable to the naked eye. As the photon flux continues to increase and the beam size continues to decrease in modern sources, there is an urgent need to better understand the effects of radiation, to incorporate these effects into analytical protocols,[37] and to understand the properties involved in radiation hardness. Nowadays, fields of application as diverse as biophotonics,[38] energy harvesting[39] or forensics[40] have opened up for innovative use of Egyptian blue in addition to its use in the arts.[41] The evolution of Egyptian blue under photon irradiation is an issue for all these applications. In the present work, we aim at identifying the effects induced by synchrotron X-ray on Egyptian blue and green pigments under usual analytical conditions. Radiation-induced effects are monitored after irradiation at increasing doses using electron paramagnetic resonance (EPR) spectroscopy.

2 Experimental section

2.1 Sample set

Two archaeological samples and two modern samples were studied. Both archaeological samples come from excavations carried out by Bernard Bruyère in Deir El Medina, Egypt in 1927 and 1935.[42] Deir El Medina is well known as a village of craftsmen working on the Royal Tombs in the Valley of the Kings at Luxor during the New Kingdom (1550–1295 BC).[43] A dozen of raw cakes of Egyptian blue and green powders were collected, including the two studied, and are now kept in the Department of Egyptian Antiquities of the Louvre Museum. Several analyses were reported by Pagès-Camagna[44] on their color, chemistry and microstructure. The blue cake no. 1 (inv. no. E 14538A, using the nomenclature of the Department of Egyptian Antiquities of the Louvre Museum) is flat with a diameter of *ca* 18 cm by 2 cm high. It has a bright blue tint (5.0 PB 5/10 in Munsell chart). The green cake no. 3 (inv. no. E 14538C) measures 12 cm in diameter by 4.5 cm in height, with a turquoise hue (7.5PB 7/6). As part of Pagès-Camagna[44] research, blue and turquoise centimetric fragments were taken from the two cakes. For the present study, approximately 50 mg of coarse powder were sampled from the two fragments. These archaeological samples are referred to as EB_a1 and EG_a3 for Egyptian blue and Egyptian green, respectively. Two modern commercial pigments (Kremer Pigmente GmbH, Aichstetten, Germany) were added to investigate the difference in reactivity between ancient and modern materials (ref. no. 10060 and 10064 for Egyptian blue and Egyptian green, respectively). The latter samples are respectively referred to as EB_K and EG_K.

2.2 Pre-characterisation of samples

The commercial samples EB_K and EG_K were studied for their morphology and elemental composition using light microscopy and scanning electron microscopy coupled to energy-dispersive X-ray spectroscopy (SEM-EDX) at IPANEMA. XRD was conducted at Institut de Recherche de Chimie Paris to characterize their structure. SEM and XRD results previously obtained by Pagès-Camagna[44] were used in this study to limit the consumption of valuable historical samples. Synchrotron-based XRF was performed at the PUMA beamline of the SOLEIL synchrotron to collect qualitative information on the elemental composition of the four pigments. Before any treatment or analysis on the samples, the powders were ground with an agate mortar in order to homogenize the particle size (few tens of micrometers observed by optical microscopy). All the experimental details and additional results are available as ESI† (ESI, Fig. S1–S5†).

2.3 Synchrotron irradiation

Irradiation at increasing doses was conducted at the PUMA beamline during two experimental sessions. Each sample was placed at 62 m from the 1.8 T wiggler source. The beam energy was set to $E = 12.5$ keV, which corresponds to the maximum flux of the beamline and is in a range of energy generally used in synchrotron experiments related to cultural heritage studies. Energy selection was done with a double crystal monochromator using Si(111) crystals in horizontal reflection geometry with an energy resolution $\Delta E/E \approx 1.5 \times 10^{-4}$ at 12.5 keV. Since the experiment was designed to simulate radiation doses and dose rates similar to those commonly used in spectroscopic experiments, we did not wish to use a broad band (pink) beam.

1266 | *J. Anal. At. Spectrom.*, 2022, **37**, 1265–1272

This journal is © The Royal Society of Chemistry 2022

A 1 m long, 600 nm iridium-covered elliptical horizontal mirror with variable bending was used to match the horizontal beam size to the sample dimensions $S = 2.8$ mm $\times$ 7 mm (horizontal $\times$ vertical). The exposed powder was irradiated at 45° with a beam intensity of $I_1 = 1.1 \times 10^{12}$ ph s^{-1}, which corresponds to a flux $\Phi_1 = \dfrac{I_1}{S} = 6 \times 10^{10}$ ph s^{-1} mm^{-2} in the first session and a beam intensity of $I_2 = 6.3 \times 10^{11}$ ph s^{-1}, corresponding to a flux $\Phi_2 = 3.2 \times 10^{10}$ ph s^{-1} mm^{-2} in the second session. More details about the beamline can be found in Tack et al.[45] Temperature (T) and relative humidity (RH) in the hutch were monitored once a day ($T = 21.3$ °C $\pm$ 0.4; RH $= 43.1\% \pm 7.6$). Pressure was considered equal to atmospheric pressure (1 atm). Two custom-made 3D printed sample holders were manufactured to obtain a volume of fully irradiated material, $V_{blue} = 2.8$ mm $\times$ 7 mm $\times$ 0.17 mm and $V_{green} = 2.8$ mm $\times$ 7 mm $\times$ 0.38 mm (width $\times$ length $\times$ depth). This was done to maximize the EPR signal intensity. However, since each irradiated volume corresponds to less than 15 mg of material, sampling of the initial pigment in small sub-volumes can lead to heterogeneity in content that will be taken into account. After irradiation, the samples were stored 50 days before EPR analysis in plastic boxes in a closed drawer at room temperature (20 °C) with a relative humidity of 47% and at atmospheric pressure.

2.4 Estimation of irradiation doses

The dose (in Gray, Gy = J kg^{-1}) received by the samples corresponds to the total amount of X-ray energy deposited in the mass of pigments contained in the irradiated volumes V_{blue} and V_{green}.[46] Dose rate is the speed at which the dose is delivered and is given in Gy s^{-1}.

Dose rate values for blue and green pigments were calculated using eqn (1):[46]

$$\dot{D} = \frac{I_{1,2} \times E \times \left(1 - e^{-l/\lambda}\right)}{\rho \times l \times S} \tag{1}$$

With $I_{1,2}$ the incident intensity (in ph s^{-1}), E the X-ray photon energy (J), l the depth in the sample (m), λ the attenuation length (m), ρ the density (kg m^{-3}) and S the beam size (m^2). The attenuation length is defined as the depth at which the X-ray intensity I drops to $I = I_0 \times 1/e$, meaning that $(1 - 1/e) \approx 63\%$ of its incident intensity was absorbed by the sample. The values for Egyptian blue $\lambda_{EB} \approx 170$ μm and green $\lambda_{EG} \approx 590$ μm were calculated following the assumptions detailed in ESI.† For the first experiment session, dose rate values of 321 Gy s^{-1} and 109 Gy s^{-1} were obtained for Egyptian blue and green respectively. For the second session, 184 Gy s^{-1} and 62 Gy s^{-1} were obtained. Finally, doses values ranging from 0.001 MGy to 69 MGy were obtained by multiplying the dose rate with the irradiation time t (s) ranging from a few seconds to a few tens of hours.

2.5 EPR spectroscopy analysis

EPR analysis was performed at the X band (9.4 GHz) using the Bruker ELEXSYS E500 spectrometer equipped with a 4122SHQE/011 resonator at Institut de Recherche de Chimie Paris. Empty 3 mm outside diameter quartz tubes (Solargil, CortecNet, Les Ulis, France) were first analyzed to check for the presence of defects originating from the tubes. Pigments before and after irradiation at increasing doses were then placed in the tubes (2–15 mg). EPR spectra were lock-in recorded with a modulation at 100 kHz of the applied magnetic field. Spectra on a large range (400 mT) were recorded with a microwave power in the range 0.2–2 mW and a field modulation amplitude 0.5 mT. Spectra over a narrower field range corresponding to paramagnetic defects were recorded with a microwave power in the range 1.25 μW to 2 mW and a modulation amplitude 0.1 mT. For all samples, spectra were both recorded at 290 K (room temperature) and at 30 K using an ESR900 helium flow cryostat (Oxford Instruments). All data processing was performed using the OriginPro software (OriginLab Corp., Northampton, MA, US). The spectra were normalised by dividing the modulation amplitude, the square root of the microwave power (W) and the sample mass (kg). A baseline was subtracted to eliminate the contribution of the background using the asymmetric least squares baseline smoothing tool. EPR intensities as a function of dose were calculated either as the double integral of the spectrum when the shape of the spectrum changed with dose (case of E' centers) or as the height of the most prominent line when the shape of the spectrum remained unchanged (case of Cu^{2+} and Al centers).

3 Results

3.1 EPR spectra of Cu^{2+} in non-irradiated Egyptian blue and green samples

The EPR spectra of the four non-irradiated samples over a wide field range are shown in Fig. 1.

The Egyptian blue samples show a characteristic spectrum of the cupric ion Cu^{2+} (d^9) in cuprorivaite CuCaSi$_4$O$_{10}$.[18,47,48] In this compound, Cu^{2+} ions are in plane square coordination with D_{4h}
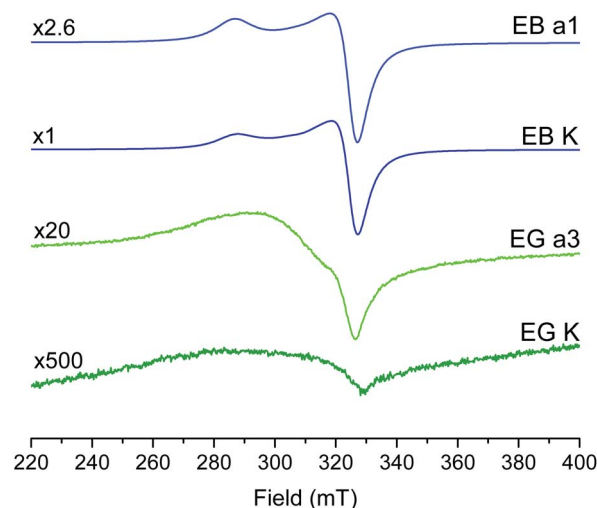

Fig. 1 EPR spectra of Cu^{2+} at 290 K in non-irradiated Egyptian blue (EB_a1, EB_K) and Egyptian green samples (EG_a3, EG_K).

This journal is © The Royal Society of Chemistry 2022

J. Anal. At. Spectrom., 2022, 37, 1265–1272 | 1267

symmetry. The eigenvalues of the g-matrix are $g_{\parallel} = 2.337 \pm 0.005$ and $g_{\perp} = 2.080 \pm 0.001$ and are typical of an unpaired electron in a $3d_{x^2-y^2}$ orbital of Cu^{2+}. The usual hyperfine interaction with central ^{63}Cu and ^{65}Cu nuclei is not observed due to exchange interactions between Cu^{2+} ions. For Egyptian green samples, slightly broader and structure-less Cu^{2+} spectra are observed. Similar spectra were reported in glassy materials.[49] The smoothing of the hyperfine structure is attributed to the broadening of the spectra by the intrinsic disorder of the glassy phase. The signal intensity is much greater for the blue samples than for the green ones, by one or two orders of magnitude. Among the green samples, the archaeological sample EG_a3 shows a much stronger intensity than the modern one EG_K. Several other paramagnetic species linked to the pigments mineralogical heterogeneity are detected in the green samples and are presented in ESI† (ESI, Fig. S6–S8†).

3.2 Radiation-induced defects in Egyptian blue samples

Upon irradiation, the color of the blue samples appears unaltered. The copper EPR signal remains unchanged both in shape and in intensity for all samples whatever the X-ray dose. This demonstrates that the copper ions remain in the Cu^{2+} form and are resistant to irradiation. After irradiation, an EPR signal is observed at room temperature at $g = 1.9986 \pm 0.0004$ for the archaeological sample EB_a1 and at $g = 1.9990 \pm 0.0002$ for the modern sample EB_K. This signal is typical of E' centers, which correspond to a hole trapped at an initially neutral oxygen vacancy linked to a silicon atom.[50] The E' centers are however produced at different doses in the two blue pigments. In EB_a1, the E' defects appear from 0.04 MGy whereas in EB_K, these defects only appear from 13 MGy (Fig. 2a and b). The E' EPR intensity at 13 MGy is about 2.5 times higher in EB_a1 than in EB_K. The non-monotonic variation in signal intensity as

a function of dose observed between 0.04 MGy and 0.4 MGy in EB_a1 can be explained by the pigment mineralogical heterogeneity. Indeed, the compounds in which defects are formed are probably present in variable proportions in the different irradiated powder samples. In addition, more in-depth analysis of EPR intensity of E' centers is hampered by the significant contribution of these defects in the quartz tube. At 30 K, both E' defects ($g = 1.9994 \pm 0.0004$) and aluminum (Al) hole centers are detected from 0.2 MGy and up to 6.6 MGy in the archaeological sample EB_a1 (Fig. 2c). An Al hole center corresponds to the formation of an electronic hole under irradiation on an oxygen close to an Al^{3+} impurity substituting a Si^{4+} ion;[51] the hole interacts with the ^{27}Al nucleus ($I = 5/2$ spin) resulting in the hyperfine splitting observed on the spectra (only the so-called perpendicular part of the Al center spectrum is shown in Fig. 2c). The EPR intensity of the Al hole center as a function of the X-ray dose is displayed in Fig. 5. It saturates from fairly low doses (about 0.4 MGy). In the modern sample EB_K, only an E' center with $g = 1.9971 \pm 0.0002$ is detected from 13 MGy up to 69 MGy but, contrary to the archaeological one, no aluminum centers are observed (Fig. 2d). As for the E' centers observed at room temperature, those detected at 30 K are created at a lower dose in the archaeological sample than in the modern one.

3.3 Radiation-induced defects in Egyptian green samples

Upon X-ray irradiation, a browning of the green samples is observed, with the intensity of the phenomenon increasing with the dose. The copper EPR signal remains unchanged both in shape and in intensity for all samples whatever the X-ray dose. This demonstrates that Cu^{2+} ions resist to irradiation and that the browning of the green samples is not linked to a change in the oxidation state of copper. After irradiation, E' ($g = 2.0027 \pm 0.0004$) and oxygen hole centers (OHC; $g = 2.0060 \pm 0.0004$, $g = 2.0097 \pm 0.0004$ and $g = 2.0136 \pm 0.0004$) are detected at

Fig. 2 Normalised EPR spectra of Egyptian blue samples irradiated at increasing doses: (a) archaeological sample EB_a1 at $T = 290$ K, (b) modern sample EB_K at $T = 290$ K, (c) and (d): same at $T = 30$ K; * points to E' defects in the quartz tube ($g = 1.9963 \pm 0.0002$ at $T = 290$ K and $g = 2.0021 \pm 0.0002$, $g = 1.9973 \pm 0.0002$, $g = 1.9953 \pm 0.0002$ at $T = 30$ K).
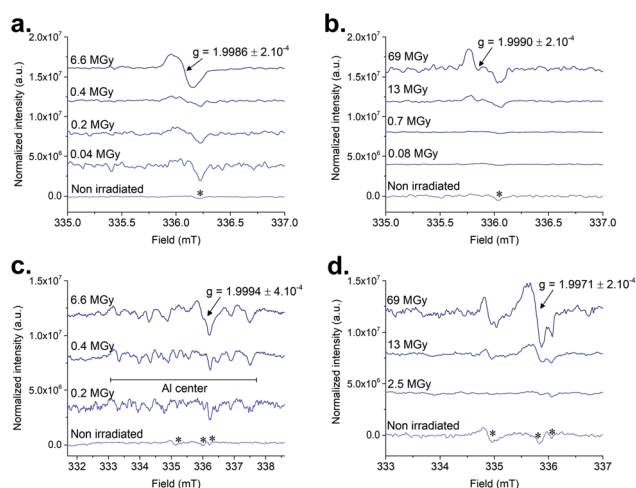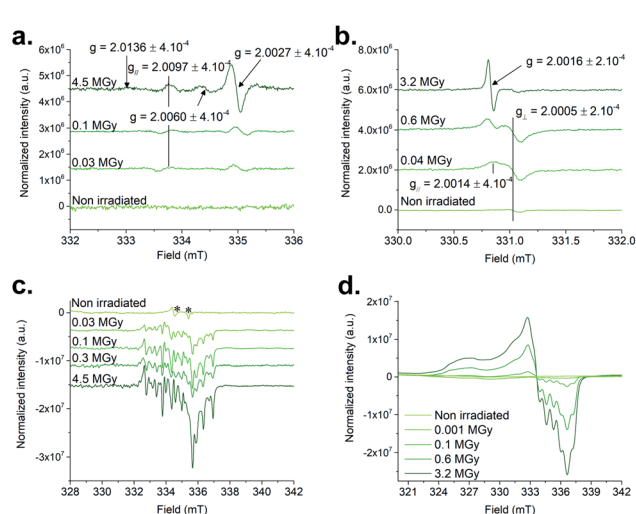

Fig. 3 Normalised EPR spectra of Egyptian green samples irradiated at increasing doses: (a) archaeological sample EG_a3 at $T = 290$ K, (b) modern sample EG_K at $T = 290$ K, (c and d) same at $T = 30$ K; * points to E' defects in the quartz tube ($g = 2.0021 \pm 0.0002$, $g = 1.9973 \pm 0.0002$).

room temperature in the archaeological green sample EG_a3 (Fig. 3a). The defects are present from 0.03 MGy and up to 4.5 MGy. For the modern sample EG_K, two types of E' centers are detected depending on the dose (Fig. 3b). At all doses, an E' center with axial g-matrix ($g_\parallel = 2.0016 \pm 0.0002$ and $g_\perp = 2.0005 \pm 0.0002$) is observed, possibly corresponding to an E'_γ center.[52] For doses above 0.6 MGy, a second E' center, possibly E'_δ, grows with an almost isotropic g-factor ($g = 2.0016 \pm 0.0002$).[52] Correlation between E' centers intensity and dose are similar for the two samples (Fig. 4). In the case of EG_a3, an abrupt increase in intensity up to 0.2 MGy is observed before a weaker growth up to 4.5 MGy, probably indicating the proximity of the saturation limit. In the case of EG_K, the intensity follows the same behavior but at higher doses. In addition, the E' defect intensity is higher for modern green than for archaeological green sample. EPR at 30 K also reveals Al centers created by X-ray irradiation in both archaeological and modern green samples (ESI, Fig. S9†). The defects appear from the minimum doses tested (0.03 MGy for EG_a3 and 0.001 MGy for EG_K) with an intensity that increases up to 3–4 MGy (Fig. 3c and d). In EG_a3, the EPR intensity of the Al centers shows a minimum at 0.3 MGy, which is not observed in the other pigments. A slight inflection is also observed on the curve of EG_K at 0.1 MGy. These non-monotonous behaviors are probably due to different concentrations of Al impurities or X-ray sensitive phases in the small amount of powder irradiated at each dose (a few milligrams). The correlation between the intensity of the Al centers and dose shows an abrupt increase in defect intensity before stabilisation towards a saturation limit for the three samples EG_a3, EG_K and EB_a1. The intensity is about 4 times higher for EG_K at 3.2 MGy than for EG_a3 at 4.5 MGy and about 30 times higher than for EB_a1 at 6.6 MGy. This suggests that there are more aluminum impurities in the modern green than in the archaeological green and much more than in the archaeological blue sample. The different paramagnetic species detected in Egyptian blue and green samples are summarized in ESI† (ESI, table S3†).

Fig. 5 Correlation between the EPR intensity of aluminum centers and X-ray dose for EG_a3, EG_K and EB_a1; the dashed line is only a visual guide.

4 Discussion

4.1 EPR as a tool for direct identification of Egyptian blue and green pigments

Egyptian blue and green pigments are often difficult to distinguish visually from each other, the green pigment having more of a turquoise hue in our modern color reference system. To give a very practical example, at the beginning of the study, the sample of Egyptian green EG_a3 was mistaken for Egyptian blue by the authors of this paper. However, both pigments exhibit notably different Cu^{2+} EPR features (Fig. 1). The blue samples have a strong Cu^{2+} signal with well resolved axial g-factor anisotropy and no hyperfine interaction, typical of the main phase $CaCuSi_4O_{10}$. The green samples show a broad Cu^{2+} signal with g-factor anisotropy and hyperfine interaction broadened by disorder, typical of the cupric ion in an amorphous phase. In addition, the intensity of the EPR signal of archaeological blue sample is five times greater than that of the green for the same sample mass, in agreement with the large difference in copper concentrations measured by SEM-EDX in previous studies: about 10–20 wto% for blue and 5 wto% for green (wto%: weight oxide percent).[15] EPR spectroscopy therefore makes it straightforward to discriminate and identify Egyptian blue and green pigments.

4.2 Radiation-induced defects

E' centers are linked to the presence of oxygen vacancies in the silica structure and are among the most common radiation-induced defects in silicates.[53] In the present study, different types of E' centers have been identified in the four samples after irradiation. At room temperature, similar E' centers are detected in both blue samples but at lower doses (0.04 MGy versus 13 MGy) and with higher intensity for EB_a1 than for EB_K. As EB_K is mainly composed of cuprorivaite with traces of wollastonite (respectively 98 wt% and 2 wt%, ESI Fig. S3†) whereas EB_a1 contains cuprorivaite but also quartz, trydimite and an amorphous phase,[44] the E' centers probably originate
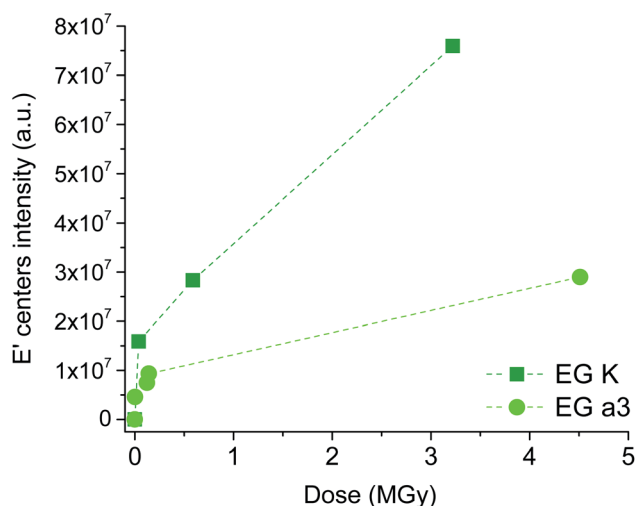

Fig. 4 Correlation between the EPR intensity of E' centers and X-ray dose in Egyptian green samples. The dashed line is only a visual guide.

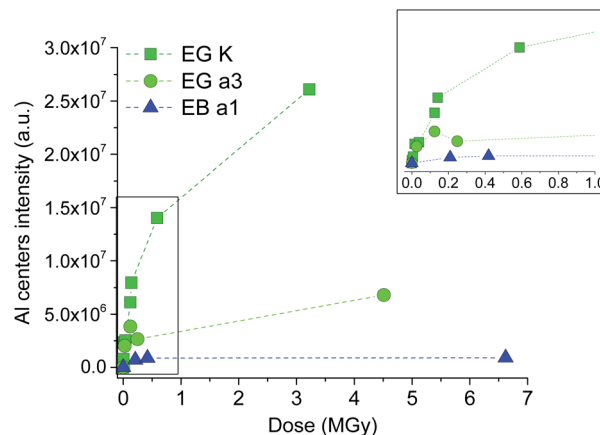This journal is © The Royal Society of Chemistry 2022

J. Anal. At. Spectrom., 2022, 37, 1265–1272 | 1269

from the silicate phases rather than from cuprorivaite. Cuprorivaite appears to be remarkably resistant to radiation. This observation could have implications for modern uses of this mineral phase in contexts where it is subjected to high dose rates or to the accumulation of doses over long periods, in a palaeo-inspired approach.[54] Different types of E' centers are detected in green samples at much lower doses than in blue samples (from 0.001 MGy). As Egyptian green samples contain an amorphous silicate phase entrapping respectively quartz and wollastonite crystals for EG_a3 (ref. 44) and quartz and trydimite crystals for EG_K (ESI, Fig. S4†), we can suppose that a large part of the defects originates from the amorphous part which is more sensitive to X-rays than the crystallised silicates compounds (quartz, wollastonite, trydimite) that are also detected in blue samples. Indeed, in amorphous materials, some chemical bonds are weaker than in a crystalline material due to structural disorder. These bonds are thus more likely to be broken by X-rays leading to the creation of defects. In addition, amorphous silica materials are more likely to include –Si–OH or –Si–O–O–Si– bonds than crystalline silicates, which are highly sensitive to radiolysis and yield oxygen hole centers or peroxy centers. Aluminum hole centers are detected in all the samples except EB_K, from 0.001 MGy for EG_K, 0.03 MGy for EG_a3 and 0.2 MGy for EB_a1. The detection of aluminum as an impurity, through the EPR-active Al center, is in line with the qualitative chemical analyses of archaeological[44] and modern samples (ESI, Fig. S1 and S5†). Finally, oxygen hole centers (OHC) are detected in the archaeological green sample EG_a3, indicating the presence of dangling oxygen atoms (with only one bond to Si instead of two).

4.3 Green pigment browning under X-ray irradiation

Egyptian green samples, whether archaeological or modern, show a browning under X-ray irradiation while blue samples do not. The fact that the EPR intensity of Cu^{2+} in green samples remains constant upon irradiation demonstrates that this browning is not related to a change in the copper oxidation state. On the other hand, browning is observed in samples where a significant amount of oxygen hole centers (OHC) and Al centers are created by irradiation. Those types of defects are known to create optical absorption bands in the visible range, at 550 nm for Al centers and at 400 and 600 nm for oxygen hole centers,[55,56] which combined with the optical absorption of Cu^{2+} would explain the browning of the green samples. The fact that the archaeological blue samples did not show any browning under irradiation despite the presence of Al centers may be related to a much lower concentration of Al centers than in the green samples (Fig. 5).

4.4 On the relevance of synchrotron X-ray analysis of Egyptian blue and green pigments

Color change, such as the browning of Egyptian green samples mentioned above, is one of the major risks of using X-rays to analyze this type of material. This is even though at least in the case of oxygen hole centers, their concentration may decrease over months, implying a partial recovery of the pigment color.[55,57] Besides, in the present study, radiation-induced damage were created by a macro-beam (a few square millimeters). Yet many studies on ancient materials are carried out with focused X-ray beams to evaluate their chemical heterogeneity, which is often structured at the micro and nano-scale.[58] These techniques concentrate all the beam intensity into a very small volume inside the sample, leading to very high local energy densities and thus to local dose depositions that are much higher than the maximum values used in this study (a ten minutes micro-beam irradiation corresponds to a dose of approximately 200 MGy for cuprorivaite, more for green). It must therefore be considered that the effects of irradiation will often be much greater than those presented in this study. Unfortunately, the detection limit of EPR analysis made it impossible to investigate materials irradiated with a microbeam because the small irradiated volume results in too little signal. To explore higher dose ranges, future studies could use white beam irradiation techniques that allow high radiation doses to be quickly accumulated in a large sample volume.

4.5 Use of defects as historical markers

EPR detection of paramagnetic defects after X-ray irradiation requires precursor defects (intrinsic or impurities) in the structure, which were EPR silent before irradiation and then made paramagnetic by capturing a hole or an electron during irradiation.[59] Therefore the occurrence of X-ray induced paramagnetic defects in Egyptian blue and green pigments should be strongly dependent on the starting materials, their purity and on the manufacturing process. This has been well illustrated in the present study as different paramagnetic defects have been highlighted between archaeological and modern samples (which have different microstructure and impurities). This opens up the exciting prospect of using radiation-induced defects as markers of the pigment history.

5 Conclusion

EPR investigation of Egyptian blue and green samples irradiated by synchrotron X-ray has evidenced the presence of radiation-induced defects (intrinsic and impurities) in all the pigments. We show that green samples are more sensitive to X-rays than blue ones, probably due to a lower radiation-hardness of the predominant amorphous phase compared to cuprorivaite which is crystallized. A browning of the green samples has been observed from the lowest doses while no color change was detected for blue. The damage threshold has thus to be evaluated according to the irradiation parameters before conducting synchrotron experiments on Egyptian green or similar type of material. Archaeological and modern samples (whether blue or green) have a different reactivity to X-rays, enjoining us not to forget the impact of impurities when modeling archaeological pigments using modern materials. We discuss the possible use of radiation-induced defects as markers of pigment history, provided that the nature and quantity of defects is correlated with the proportion of the

different phases composing the pigment, the nature and purity of the reagents and the pigment processing parameters.

Conflicts of interest

There are no conflicts to declare.

Notes and references

1 S. Colinart, E. Delange and S. Pagès, *Technè*, 1996, 29–45.
2 I. Shaw, *The Oxford History of Ancient Egypt*, Oxford University Press, Oxford, 2003, pp. 479–483.
3 H. Jaksch, W. Seipel, K.-L. Weiner and A. El Goresy, *Naturwissenschaften*, 1983, **70**, 525–535.
4 S. Pagès-Camagna, E. Laval, D. Vigears and A. Duran, *Appl. Phys. A: Mater. Sci. Process.*, 2010, **100**, 671–681.
5 J. Riederer, in *Egyptian Blue*, edn E. W. Fitzhugh, Oxford University Press, Oxford, UK, 1997, vol. 3, pp. 23–40.
6 M. C. Gaetani, U. Santamaria and C. Seccaroni, *Stud. Conserv.*, 2004, **49**, 13–22.
7 M. Aceto, E. Calà, G. Fenoglio, M. Labate, C. Denoël, L. Operti and A. Agostino, *J. Archaeol. Sci. Rep.*, 2020, **33**, 102487.

8 J. Bredal-Jørgensen, J. Sanyova, V. Rask, M. L. Sargent and R. H. Therkildsen, *Anal. Bioanal. Chem.*, 2011, **401**, 1433–1439.
9 M. Ganio, J. Salvant, J. Williams, L. Lee, O. Cossairt and M. Walton, *Appl. Phys. A: Mater. Sci. Process.*, 2015, **121**, 813–821.
10 G. A. Mazzocchin, F. Agnoli and I. Colpo, *Anal. Chim. Acta*, 2003, **478**, 147–161.
11 M. C. Edreira, M. J. Feliu, C. Fernández-Lorenzo and J. Martín, *Helv. Chim. Acta*, 2003, **86**, 29–49.
12 J.-A. Chaptal, *Mémoires de la Classe des Sciences Mathématiques et Physiques de l'Institut de France*, 1809, pp. 229–235.
13 F. Fouqué, *Bull. Soc. Fr. Mineral.*, 1889, **12**, 36–38.
14 P. Baraldi, F. Bondioli, C. Fagnano, A. M. Ferrari, A. Tinti and M. Vinella, *Ann. Chim.*, 2001, **91**, 679–692.
15 S. Pagès-Camagna and S. Colinart, *Archaeometry*, 2003, **45**, 637–658.
16 A. Bloise, S. Abd El Salam, R. De Luca, G. Crisci and D. Miriello, *Appl. Phys. A: Mater. Sci. Process.*, 2016, **122**, 1–8.
17 M. Tite, M. Bimson and M. Cowell, in *Technological Examination of Egyptian Blue*, edn J. B. Lambert, ACS Publications, Chicago, USA, 1984, vol. 3, pp. 215–242.
18 P. Mirti, L. Appolonia, A. Casoli, R. Ferrari, E. Laurenti, A. A. Canesi and G. Chiari, *Spectrochim. Acta, Part A*, 1995, **51**, 437–446.
19 G. Mazzocchin, F. Agnoli, S. Mazzocchin and I. Colpo, *Talanta*, 2003, **61**, 565–572.
20 M. Nicola, L. M. Seymour, M. Aceto, E. Priola, R. Gobetto and A. Masic, *Archaeol. Anthropol. Sci.*, 2019, **11**, 5377–5392.
21 D. A. Scott, *Stud. Conserv.*, 2016, **61**, 185–202.
22 M. S. Tite, *Archaeometry*, 1987, **29**, 21–34.
23 P. Bianchetti, F. Talarico, M. G. Vigliano and M. F. Ali, *J. Cult. Herit.*, 2000, **1**, 179–188.
24 C. Grifa, L. Cavassa, A. De Bonis, C. Germinario, V. Guarino, F. Izzo, I. Kakoulli, A. Langella, M. Mercurio and V. Morra, *J. Am. Ceram. Soc.*, 2016, **99**, 3467–3475.
25 L. Bertrand, M. Cotte, M. Stampanoni, M. Thoury, F. Marone and S. Schöder, *Phys. Rep.*, 2012, **519**, 51–96.
26 S. Pagès-Camagna, I. Reiche, C. Brouder, D. Cabaret, S. Rossano, B. Kanngiesser and A. Erko, *Xray Spectrom.*, 2006, **35**, 141–145.
27 C. Calza, M. Anjos, S. Mendonça de Souza, A. Brancaglion Jr and R. Lopes, *Appl. Phys. A: Mater. Sci. Process.*, 2007, **90**, 75–79.
28 D. Lau, P. Kappen, M. Strohschnieder, N. Brack and P. J. Pigram, *Spectrochim. Acta, Part B*, 2008, **63**, 1283–1289.
29 A. Kostomitsopoulou Marketou, F. Giannici, S. Handberg, W. De Nolf, M. Cotte and F. Caruso, *Anal. Chem.*, 2021, **93**, 11557–11567.
30 T. Pradell, N. Salvado, G. D. Hatton and M. S. Tite, *J. Am. Ceram. Soc.*, 2006, **89**, 1426–1431.
31 L. Bertrand, S. Schöder, D. Anglos, M. B. Breese, K. Janssens, M. Moini and A. Simon, *Trac. Trends Anal. Chem.*, 2015, **66**, 128–145.

This journal is © The Royal Society of Chemistry 2022

J. Anal. At. Spectrom., 2022, **37**, 1265–1272 | **1271**

32 C. Gervais, M. A. Languille, S. Réguer, M. Gillet, E. P. Vicenzi, S. Chagnot, F. Baudelet and L. Bertrand, *Appl. Phys. A: Mater. Sci. Process.*, 2013, **111**(1), 15–22.

33 L. Monico, M. Cotte, F. Vanmeert, L. Amidani, K. Janssens, G. Nuyts, J. Garrevoet, G. Falkenberg, P. Glatzel, A. Romani, *et al.*, *Anal. Chem.*, 2020, **92**, 14164–14173.

34 A. Gimat, S. Schoeder, M. Thoury, M. Missori, S. Paris-Lacombe and A.-L. Dupont, *Biomacromolecules*, 2020, **21**, 2795–2807.

35 M. Moini, C. M. Rollman and L. Bertrand, *Anal. Chem.*, 2014, **86**, 9417–9422.

36 G. D. Richards, R. S. Jabbour, C. F. Horton, C. L. Ibarra and A. A. MacDowell, *Am. J. Phys. Anthropol.*, 2012, **149**, 172–180.

37 Netherlands Institute for Conservation, *Art and Science, Irradiation Passport for Art*, **https://www.nicas-research.nl/projects/irradiation-passport-for-art/**, Accessed: 2020-11-27.

38 G. Selvaggio, A. Chizhik, R. Nißler, D. Meyer, L. Vuong, H. Preiß, N. Herrmann, F. A. Mann, Z. Lv, T. A. Oswald, *et al.*, *Nat. Commun.*, 2020, **11**, 1–11.

39 P. Berdahl, S. K. Boocock, G. C.-Y. Chan, S. S. Chen, R. M. Levinson and M. A. Zalich, *J. Appl. Phys.*, 2018, **123**, 1–11.

40 B. Errington, G. Lawson, S. W. Lewis and G. D. Smith, *Dyes Pigm.*, 2016, **132**, 310–315.

41 R. Fontana, P. Baraldi, M. E. Fedi, M. Galeotti, S. Omarini, P. Zannini and J. Striova, *J. Cult. Herit.*, 2020, **45**, 370–378.

42 B. Bruyère and G. Jourdain, *Rapport sur les fouilles de Deir El Médineh (1934-1935) – Troisième partie, Le village, les décharges publiques, la station de repos du col de la Vallée des Rois*, Institut français d'archéologie orientale technical report, 1939.

43 N. Grimal, *Histoire de l'Égypte ancienne*, Fayard, Paris, France, 2014, p. 370.

44 S. Pagès-Camagna, PhD thesis, Université de Marne-la-Vallée, France, 1999.

45 P. Tack, B. Bazi, B. Vekemans, T. Okbinoglu, F. Van Maldeghem, S. Goderis, S. Schoeder and L. Vincze, *J. Synchrotron Radiat.*, 2019, **26**, 2033–2039.

46 M. Van Schooneveld and S. DeBeer, *J. Electron Spectrosc. Relat. Phenom.*, 2015, **198**, 31–56.

47 R. J. Ford and M. A. Hitchman, *Inorg. Chim. Acta*, 1979, **33**, L167–L170.

48 E. F. Orsega, F. Agnoli and G. Mazzocchin, *Talanta*, 2006, **68**, 831–835.

49 C. L. Marquardt, *Appl. Phys. Lett.*, 1976, **28**, 209–211.

50 R. Weeks, *J. Appl. Phys.*, 1956, **27**, 1376–1381.

51 J. H. Mackey, J. W. Boss and D. E. Wood, *J. Magn. Reson.*, 1970, **3**, 44–54.

52 D. Griscom and E. Friebele, *Phys. Rev. B*, 1986, **34**, 7524–7533.

53 A. Alessi, S. Agnello, G. Buscarino, Y. Pan and R. I. Mashkovtsev, *Applications of EPR in Radiation Research*, Springer, New York, USA, 2014, pp. 255–295.

54 L. Bertrand, C. Gervais, A. Masic and L. Robbiola, *Angew. Chem., Int. Ed.*, 2018, **57**, 7288–7295.

55 J. Sheng, K. Kadono and T. Yazawa, *Appl. Radiat. Isot.*, 2002, **57**, 813–817.

56 C. Shao, W. Xu, N. Ollier, M. Guzik, G. Boulon, L. Yu, L. Zhang, C. Yu, S. Wang and L. Hu, *J. Appl. Phys.*, 2016, **120**, 1–8.

57 J. Sheng, X. Yang, W. Dong and J. Zhang, *Int. J. Hydrogen Energy*, 2009, **34**, 3988–3991.

58 L. Bertrand, L. Robinet, M. Thoury, K. Janssens, S. X. Cohen and S. Schöder, *Appl. Phys. A: Mater. Sci. Process.*, 2012, **106**, 377–396.

59 C. D. Marshall, J. A. Speth and S. A. Payne, *J. Non-Cryst. Solids*, 1997, **212**, 59–73.

1272 | *J. Anal. At. Spectrom.*, 2022, **37**, 1265–1272

This journal is © The Royal Society of Chemistry 2022